https://doi.org/10.5194/egusphere-2025-5122
Preprint. Discussion started: 24 November 2025

Spatio-temporal Monitoring of Agricultural Drought in China Based on Downscaled Soil Moisture Data

Xiaoyu Luo[1,2], Mengmeng Cao[1,2*], Yaoping Cui[1,2*], Xiangjin Meng[3], Yan Zhou[1,2], Yibo Yan[4]

[1]College of Geographical Sciences, Faculty of Geographical Science and Engineering, Henan University, Zhengzhou 450046, China

[2]Key Laboratory of Geospatial Technology for the Middle and Lower Yellow River Regions, Ministry of Education, Henan University, Kaifeng 475004, China

[3]Key Laboratory of Lake and Watershed Science for Water Security, Nanjing Institute of Geography and Limnology, Chinese Academy of Sciences, Nanjing 210008, China

[4]College of Global change and Earth System Science, Beijing Normal University, Beijing 100875, China

Correspondence: Mengmeng Cao (mmengcao@henu.edu.cn) & Yaoping Cui (cuiyp@lreis.ac.cn)

Abstract: Agricultural drought threatens China's food and ecological security, and accurate spatio-temporal monitoring is key for disaster mitigation. Soil moisture is critical for drought assessment, but the accuracy of existing remote sensing-based SM products in China remains to be improved. This study develops a framework that synergistically integrates a spatiotemporally adaptive gap-filling algorithm with a machine learning-based downscaling approach, generating a seamless 0.05∘ monthly SM dataset for China from 2003 to 2023. The methodology harnesses the complementary strengths of random forest modeling and spatiotemporal reconstruction techniques to effectively fuse multi-source satellite observations, achieving dual improvements in SM data accuracy and spatial coverage. Using this dataset, the standardized soil moisture index was applied to characterize the spatio-temporal evolution of agricultural drought. Results demonstrate that (1) The downscaled SM dataset achieves significant improvements in both spatial resolution and accuracy, showing a 2.3–34.4% reduction in ubRMSE and 1.2–52.7% improvement in correlation coefficients compared to benchmark datasets. (2) Drought characterization based on the downscaled SM dataset and SSI accurately identified the extent of agricultural drought, showing a significant spatiotemporal consistency with agricultural disaster area. (3) Agricultural drought intensified significantly across China during the study period, characterized by northward migration of drought center and spatially heterogeneous aridification patterns — decreasing severity from northwest to southeast while increasing from northeast to southwest. High-frequency drought zones were predominantly clustered in ecologically vulnerable regions, particularly the agro-pastoral ecotone of northern China. (4) Distinct intra-annual drought dynamics emerged, with a southwest-to-northeast expansion dominating from January to June, followed by bidirectional propagation from the Yellow River-Huaihe River Basin (YRB-HRB) to northwestern and southeastern regions from June to December. This study provides high-accuracy data support for agricultural drought monitoring and offers scientific insights for developing regional differentiated drought mitigation strategies, which are of great significance for ensuring national food security.

Keywords: Drought monitoring, Soil moisture, Spatiotemporal analysis, China

1.Introduction

Drought, recognized as one of the most widespread and economically devastating natural disasters globally, is characterized by its prolonged duration, extensive spatial coverage, and severe impacts on

https://doi.org/10.5194/egusphere-2025-5122
Preprint. Discussion started: 24 November 2025

agricultural productivity and national economic stability (Yang et al., 2021). China, with its vast agricultural sector, remains particularly susceptible to recurrent droughts. Annually, approximately 3×10^7 hm^2 of cropland in China are affected by drought, leading to grain yield losses estimated at $3–5\times10^{10}$ kg per year, which positions drought as one of most impactful natural disasters on agricultural production (Liu et al., 2021; Wang, 2010). Therefore, accurate monitoring of agricultural drought is essential for mitigating crop yield reduction and ensuring national food security.

Agricultural drought assessment primarily relies on three categories of indicators: meteorological indices, soil moisture indices, and crop physiological-ecological indices (Sridhar et al., 2008; Bodner et al., 2015). Meteorological indices, predominantly derived from precipitation data, are effective detecting climatic anomalies. However, their poor correlation with actual crop water stress, largely due to their limited representation of land-atmosphere interactions, restricts their utility for agricultural drought assessment (Aiguo, 2011). While crop physiological-ecological indices directly quantify plant water status, their operational implementation is constrained by heavy reliance on intensive field measurements, posing challenges for generating spatially consistent and temporally continuous datasets (Hansen and Jones, 2000; White et al., 2012). In contrast, soil moisture (SM) indices are more directly linked to crop water availability, as root-zone soil water content directly governs plant water uptake. Therefore, SM is widely recognized as a key variable for quantifying agricultural drought severity (Dai, 2011).

SM can primarily be estimated through two approaches: in-situ observations and remote sensing retrievals (Ochsner et al., 2013). While in-situ observations provide high accuracy measurements at specific sites, their sparse and uneven spatial distribution hinders comprehensive characterization of regional SM heterogeneity. Remote sensing retrievals have emerged as a dominant methodology for large-scale SM monitoring, owing to their unparalleled advantages in spatial coverage continuity and temporal observation persistence. Among various remote sensing modalities, microwave remote sensing, especially passive microwave techniques, has been widely utilized for acquiring SM data at both global and regional scales (Ding et al., 2024). This is attributed to their sensitivity to soil permittivity, all-day and all-weather operational capability, and moderate penetration through vegetation canopies and soil layers (Konings et al., 2019). For instance, the Advanced Microwave Scanning Radiometer- Earth Observing System (AMSR-E) generated global SM retrievals from 2002 to 2011 through multi-frequency C/X-band observations (6.9–10.7 GHz) with dual-polarization channels. Its successor, the Advanced Microwave Scanning Radiometer 2 (AMSR2), launched in 2012, continues to provide similar observations (Imaoka et al., 2010). Concurrently, the Soil Moisture and Ocean Salinity Mission (SMOS) has delivered continuous L-band (1.4 GHz) radiometric measurements since 2010, which are particularly valuable for SM estimation due to their reduced sensitivity to vegetation opacity. More recently, the Soil Moisture Active Passive (SMAP) mission, launched in 2015, combines L-band passive and active microwave observations (though the active component failed), further enhancing the quality and resolution of global SM products. However, passive microwave systems fundamentally detect the weak thermal emission (brightness temperature) from the land surface (Meng et al., 2024). This inherent characteristic necessitates large antenna sizes to achieve sufficient signal-to-noise ratio, consequently leading to observations with coarse spatial resolution (typically ranging from dozens of kilometers). This coarse resolution severely limits their applicability for agricultural drought monitoring, as fine-scale or file-scale SM information is crucial for accurate assessments and localized assessments (Piles et al., 2014). To address this inherent limitation, various spatial downscaling technologies have been

https://doi.org/10.5194/egusphere-2025-5122
Preprint. Discussion started: 24 November 2025

developed to enhance the spatial resolution of passive microwave SM products, typically to finer resolutions ranging from 25 to 50 km. These approaches are typically classified into three main categories: empirical methods, semi-empirical methods, and physical methods (Fuentes et al., 2022; Song et al., 2024; Zhong et al., 2024).

Empirical downscaling methods primarily rely on observed data and prior knowledge to establish statistical relationships between SM and scale factors. Common techniques include polynomial regression, geographically weighted regression (GWR) and spatial interpolation (Yao et al., 2013; Dong et al., 2020; Mohseni et al., 2023). Although these methods are computationally efficient and straightforward to implement, their lack of explicit physical constraints and the subjectivity in selecting or parameterizing the statistical relationships often limit their robustness and transferability across different regions or conditions. In contrast to empirical methods, semi-empirical approaches attempt to integrate simplified physical principles into empirical frameworks by incorporating process-based constraints. A prominent example is the Disaggregation based on Physical and Theoretical Scale Change (DISPATCH) method, which synergizes physical insights with statistical formulations to enhance interpretability while maintaining operational efficiency (Malbéteau et al., 2016). Physically based downscaling techniques, compared to empirical and semi-empirical methods, offer a more explicit representation of the interactions between surface variables and microwave signals. These methods typically involve the assimilation of coarse-resolution SM data into land surface or hydrological models augmented with high-resolution ancillary inputs (Merlin et al., 2012). Despite their strong mechanistic fidelity, the accuracy of these models can be significantly impacted by structural uncertainties and inaccuracies in input parameters (Peng et al., 2017).

Despite advancements in SM downscaling methodologies and the proliferation of global SM products, their application in agricultural drought monitoring across China remains hindered by several critical limitations (Liu et al., 2022; Song et al., 2022). Firstly, many downscaling algorithms are developed with specific surface characteristics or climatic regimes in mind, leading to strong regional dependencies that restrict their generalizability across China's diverse agro-ecological landscapes. Secondly, the spatio-temporal continuity of existing downscaled SM products is frequently compromised by orbital gaps, cloud contamination, and retrieval uncertainties, resulting in significant data discontinuities that undermine their operational utility. Thirdly, several global or continental SM datasets exhibit limited accuracy over China, further constraining their reliability for timely and precise drought monitoring. To address these limitations, we developed a novel integrative framework that synergizes multi-source satellite observations (AMSR-E/2, SMOS, MODIS) with in-situ measurements. This framework incorporates a spatiotemporally adaptive gap-filling algorithm to ensure data continuity and a robust machine learning-based downscaling model to generate seamless 0.05° resolution monthly SM data spanning 2003–2023. We further used standardized soil moisture indices (SSI) to achieve accurate mapping from SM dynamics to agricultural drought characterization, and examined the spatiotemporal dynamics of agricultural drought in China. This research is anticipated to provides crucial scientific support for national drought risk assessment, inform adaptive agricultural management, and aid in developing effective drought mitigation strategies for China.

https://doi.org/10.5194/egusphere-2025-5122
Preprint. Discussion started: 24 November 2025

2.Materials and methods

2.1. Study area

China, has an area of 9.6×10⁶ km² and is in eastern Asia, encompassing a latitudinal range from 6°19′N to 53°33′N and a longitudinal span from 73°33′E to 135°05′E. Its terrain exhibits a prominent west-to-east gradient of declining elevation, forming a distinct three-tiered topographic hierarchy that profoundly influences regional climate and hydrology. Climatically, China encompasses subtropical monsoonal, temperate continental, and alpine regimes, with precipitation patterns decreasing systematically from southeast to northwest. Given China's vast geographical expanse and topographic complexity, pronounced spatial variations in temperature, precipitation, and SM exist across its diverse regions. To elucidate the agricultural drought characteristics across China, the study area was divided into nine river basins. This classification is guided by the spatial structure of river networks and informed by key geographic and climatic factors, including topography, precipitation patterns, and regional climate regimes. The delimited basins include the Song-Liao River Basin (SLRB), the Hai River Basin (HRB), the Yellow River Basin (YRB), the Huai River Basin (HRYB), the Yangtze River Basin (CRB), the Pearl River Basin (PRB), the Southeast Rivers Basin (SERB), the Southwest Rivers Basin (SWRB), and the Inland River Basin (NWRB). The spatial distribution of the nine basins is shown in Fig. 1.

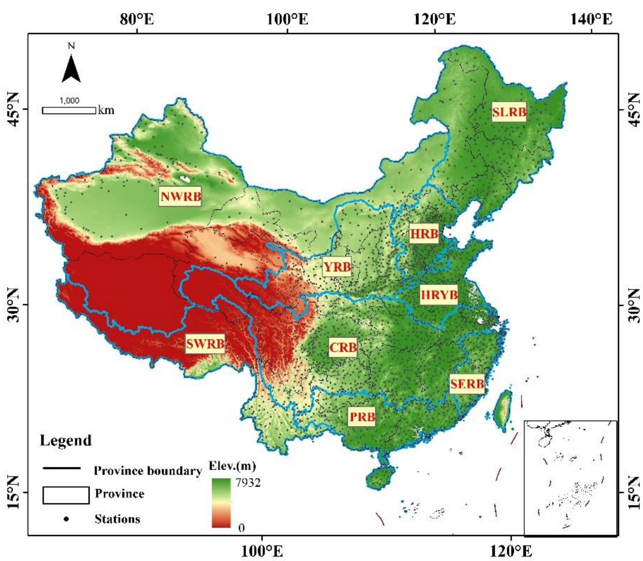

Fig. 1. Overview of the study area and nine major river basins in China, overlaid with in-situ SM distribution

2.2. Data

2.2.1. SM data

To generate a continuous monthly SM dataset across China for the period 2002–2023, we integrated satellite- and ground-based observations. We used Level-3 monthly products from AMSR-E on-board the Aqua satellite (July 2002–September 2011) and AMSR2 on-board the GCOM-W1 satellite (July 2012–December 2023). Both datasets have a spatial resolution of 25 km

https://doi.org/10.5194/egusphere-2025-5122
Preprint. Discussion started: 24 November 2025

and are expressed in volumetric units (m³/m³). To bridge the observational gap between AMSR-E and AMSR2, we used the SMOS-IC V105 daily product (July 2011–December 2012), which was aggregated to a monthly scale. This product helps to fill the data gap during the transition period between the two main satellite datasets.

For validation, we utilized in situ SM measurements obtained from the common application support platform for land observation satellite, China's national meteorological stations and China's agrometeorological and ecological observation network (January 2003–December 2023). Hourly 0–10 cm depth observations were averaged across the four time points closest to satellite overpasses to derive monthly values, with outliers excluded through rigorous quality control.

Two widely used reconstructed SM products were adopted as baseline datasets for accuracy comparison: (1) PI (Zhang et al., 2023): Developed by integrating multiple datasets and machine learning, this dataset delivers global daily SM data at a 1-km resolution (2000–2020), showing an unbiased root mean square error (ubRMSE) ranging from 0.033–0.048 m³/m³ with independent SM networks. (2) PII (Meng et al., 2021): Produced using a reconstruction model-based downscaling technique that integrates SM data from various passive microwave products, this dataset provides monthly SM estimates at a 0.25° resolution across China (2002–2018), with an ubRMSE ranging from 0.036 to 0.048 m³/m³ when compared to in situ measurements.

2.2.2. Auxiliary data

The multi-source geospatial datasets utilized in the SM downscaling model are summarized in Table 1, with detailed descriptions of data sources and spatiotemporal resolutions. MODIS monthly products (2003–2023), including land surface temperature (LST), leaf area index (LAI), and normalized difference vegetation index (NDVI), were obtained from National Aeronautics and Space Administration at a 0.05° resolution. These vegetation and land surface parameters were processed by averaging daytime and nighttime observations, removing outliers via first-order differencing, and interpolating missing values using Savitzky-Golay filtering to ensure temporal continuity (Kandasamy et al., 2013). Meteorological parameters (2m temperature, total evaporation, total precipitation, and surface net solar radiation) were obtained from the European Centre for Medium-Range Weather Forecasts (ECMWF) at a 0.1° spatial resolution and monthly temporal resolution (2003–2023). Topographic data comprised elevation from the Shuttle Radar Topography Mission (SRTM) 1 km digital elevation model (DEM), resampled to 0.05°, and slope derived through a 3×3 neighborhood gradient algorithm. Land cover data is the MODIS Collection 6 global land cover product. This dataset provides annual land cover maps at 500 m spatial resolution based on the 17-class International Geosphere Biosphere Program classification scheme.

For validation, provincial-scale agricultural drought indicators (2003–2023) – including crop disaster areas and crop coverage - were extracted from the China National Statistical Yearbook and normalized against regional arable land statistics.

Table 1 Overview of the datasets used in this study.

Datsets	Satellite	Spatial coverage	Spatial/temporal resolution	Dates	Notes
AMSR-E L3	Aqua	Global	0.25°,1 monthy	2002 - 2011	SM
AMSR-2 L3	GCOM-W1	Global	0.25°,1 monthy	2012 - 2023	SM
SMOS-IC	SMOS	Global	0.25°,1 monthy	2011 - 2012	SM
MYD11C3	Aqua	Global	0.05°,1 monthy	2003 - 2023	LST
MYD13C2	Aqua	Global	0.05°,1 monthy	2003 - 2023	NDVI

https://doi.org/10.5194/egusphere-2025-5122
Preprint. Discussion started: 24 November 2025

MYD15	Aqua	Global	0.05°,1 monthy	2003 - 2023	LAI
MCD12Q1	MODIS	Global	500 m, yearly	2003 - 2023	Land cover
ECMWF	-	Global	0.1°,1 monthy	2003 - 2023	Auxiliary data
SRTM	-	Global	Resample 0.05°	2003 - 2023	DEM,Slope
Station	-	China	site data, daily	2003 - 2023	SM
Validation	-	China	-	2003 – 2023	Agricultural
Data	-	-	-	-	drought indicators
PI	-	Global	0.1°, daily	2000 - 2020	benchmark dataset
PII	-	China	0.05°, monthy	2002 - 2018	benchmark dataset

3.Method

Fig. 2 outlines the three-stage methodological framework designed to derive fine-resolution agricultural drought diagnostics. Stage 1: Gap-filling of passive microwave SM products – A spatiotemporally adaptive gap-filling algorithm was developed to address data gaps in multi-sensor passive microwave SM observations (AMSR-E, SMOS, and AMSR2). This algorithm synergistically couples the enhanced Savitzky-Golay filter for temporal smoothing, GWR for spatial consistency reconstruction, and least squares regression for fitted interpolation and cross-sensor calibration, generating a continuous SM dataset across China from 2003 to 2023. Stage 2: Data-driven SM downscaling – A machine learning-based downscaling model was established by integrating SM-related environmental covariates, including vegetation dynamics, land surface parameters, meteorological parameters and topographic controls. Through iterative feature selection and random forest algorithm, the model produced monthly seamless SM datasets at 0.05° spatial resolution. Stage 3: Agricultural drought mapping – SSI was used to establish robust quantitative links between SM dynamics and agricultural drought patterns, enabling a systematic analysis of the spatio-temporal evolution of drought conditions across China during 2003-2023.

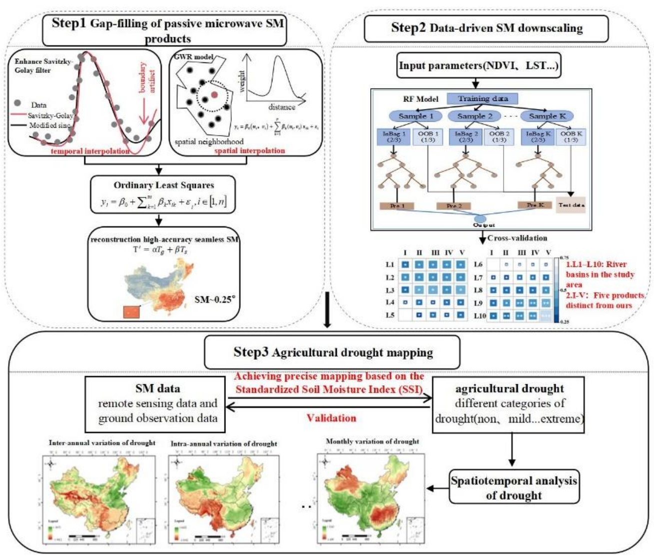

Fig. 2. The overall methodological framework of this study.

https://doi.org/10.5194/egusphere-2025-5122
Preprint. Discussion started: 24 November 2025

3.1. Construction of spatio-temporally seamless SM Product

3.1.1. Reconstruction of missing values in passive microwave remote sensing data

To reconstruct missing SM pixels by leveraging spatio-temporal information, we implemented a three-step hybrid approach. First, an enhanced Savitzky-Golay filter and the GWR method were used to integrate spatio-temporal information for the preliminary reconstruction of missing SM values. Second, least squares regression was applied to optimize the initial reconstruction, which effectively minimized inter-sensor biases and recovered SM values. Finally, a harmonized SM dataset spanning 2003–2023 was constructed by merging AMSR-E, SMOS, and AMSR2 observations, ensuring spatiotemporal continuity across heterogeneous landscapes.

（1）enhanced Savitzky-Golay filtering algorithm

Due to limitations in retrieval algorithms and atmospheric disturbances such as cloud cover, remotely sensed SM products commonly exhibit spatio-temporal discontinuities. Although monthly SM composites based on valid observations reduce missing data to some extent, substantial gaps still exist. The Savitzky-Golay filter, a local polynomial regression technique based on least-squares fitting within a moving window, has been widely used for reconstructing missing values in time-series data. It fits a high-order polynomial over local windows to smooth the time series and estimate missing values for the preliminary reconstruction of missing SM data (Chen et al., 2021). However, traditional Savitzky-Golay filtering suffers from poor noise suppression beyond the cutoff frequency and generates significant artifacts near data boundaries. To overcome these limitations, we adopted an enhanced Savitzky-Golay filtering method (Schmid et al., 2022). This improved filter introduces two key modifications: (i) a window function is used as the fitting weight to enhance high-frequency noise suppression; and (ii) a convolution kernel based on the sinc function with Gaussian-like windowing is employed to reduce artifacts near data boundaries. For a given pixel time series Y with missing SM values, the reconstructed time series Y_j^* can be derived using formula (1).

$$Y_j^* = \frac{\sum_{i=-m}^{m} W_i C_i Y_{j+i}}{N} \tag{1}$$

where W_i denotes the weight of the Gaussian window function, C_i represents the modified filter coefficient, m is the half-width of the moving window, and N is the number of convolution terms, equal to the full window size $(2m+1)$.

（2）GWR model

GWR constructs localized regression models for each observation point based on its surrounding neighboring values, and has been widely recognized as a robust approach for estimating missing spatial data (Cao et al., 2021). We adopted the GWR approach to reconstruct missing pixels once their locations were identified. By incorporating local spatial relationships and neighboring pixel values into the regression framework, GWR enables the interpolation of missing SM data, effectively filling gaps in the dataset while preserving the spatial heterogeneity of soil moisture patterns. The GWR model estimates the missing SM value y_i at location (u_i, v_i) using the following form:

$$y_i = \beta_0(u_i,\ v_i) + \sum_{k=1}^{p} \beta_k(u_i, v_i)\, x_{ik} + \varepsilon_i \tag{2}$$

Where x_{ik} represents the SM value of the k^{th} neighboring pixel within a local spatial window (15×15 pixels centered on the target), $\beta_0(u_i, v_i)$ is the local intercept, $\beta_k(u_i, v_i)$ denotes the local slope corresponding to the k^{th} neighbor, and ε_i is the residual error. Model parameters are

https://doi.org/10.5194/egusphere-2025-5122
Preprint. Discussion started: 24 November 2025

estimated using a weighted least squares method:

$$\beta(u_i,\ v_i) = \left(X^T W(u_i,\ v_i) X\right)^{-1} X^T W(u_i,\ v_i) Y \tag{3}$$

Where $\beta(u_i, v_i)$ is the vector of locally estimated regression coefficients. $W(u_i, v_i)$ is the spatial weighting matrix. X and Y denote the explanatory and response variables within the local neighborhood. The weight of each neighboring pixel decreases with increasing distance from the focal cell, reflecting spatial dependence.

An in-depth analysis of SM data revealed that spatially adjacent pixels with similar meteorological conditions tend to exhibit consistent SM dynamics, allowing for more reliable estimations based on their collective information (Peng et al., 2017). To ensure higher reconstruction accuracy, we assessed the environmental similarity of pixels within the window and assigned greater weights to similar pixels. Through sensitivity tests conducted on selected similar pixels, we found that setting the parameter $M_g = 3$ during calculations yielded more accurate estimations of the SM values for missing pixels. This optimal value of Mg strikes a balance between incorporating enough similar pixels to capture the underlying spatial patterns and avoiding the inclusion of too many dissimilar ones that could introduce noise. Consequently, the weights were determined using Formulas 4 and 5.

$$D = \sqrt{(u_i - u_k)^2 + (v_i - v_k)^2} \tag{4}$$

$$W_k = \frac{\frac{M_c}{D_k}}{\sum_{k=1}^{m} \frac{M_c}{D_k} + \sum_{j=1}^{n} \frac{M_g}{D_j}} \quad W_j = \frac{\frac{M_g}{D_j}}{\sum_{k=1}^{m} \frac{M_c}{D_k} + \sum_{j=1}^{n} \frac{M_g}{D_j}} \tag{5}$$

Where D is the Euclidean distance between a neighboring pixel and the missing target. j and k denote similar and general neighbors within the window. W_j and W_k are their corresponding weights, and $M_g = 3, M_c = 1$ are the fixed weighting factors for similar and non-similar neighbors, respectively.

（3）Optimizing refined reconstruction outcomes of the enhanced Savitzky-Golay Filtering Algorithm and GWR model

To further improve the accuracy of SM reconstruction, we integrated the spatio-temporal information derived from the Savitzky-Golay filtering and GWR methods through a weighted least-squares fusion strategy. The final reconstructed SM value T' was expressed as a linear combination of the GWR and Savitzky-Golay derived values:

$$\mathrm{T}' = \alpha T_g + \beta T_s \tag{6}$$

Where T' denotes the integrated SM estimate. T_g and T_s are the SM values reconstructed using the GWR and Savitzky-Golay methods, respectively. and α and β are the corresponding weighting coefficients.

To estimate the optimal values of α and β, we selected a subset of valid pixels from each image. These pixels were interpolated using both GWR and Savitzky-Golay methods. Subsequently, the least squares method was applied to fit the data obtained from the two methods, yielding the fitting coefficients (Formula 7).

$$\Delta\mathrm{T}(\alpha, \beta) = \sum_{i=1}^{n} [T_i - T_i']^2 \tag{7}$$

where T_i is the valid SM value at pixel i, and T_i' is the reconstructed value based on the weighted

https://doi.org/10.5194/egusphere-2025-5122
Preprint. Discussion started: 24 November 2025

combination. The optimal coefficients were derived by minimizing ΔT using the following partial derivatives:

$$\frac{\partial \Delta T(\alpha,\beta)}{\partial \beta} = -2\sum_{i=1}^{n}(T_i - \alpha T_g - \beta T_k)T_g = 0 \tag{8}$$

$$\frac{\partial \Delta T(\alpha,\beta)}{\partial \beta} = -2\sum_{i=1}^{n}(T_i - \alpha T_g - \beta T_k)T_k = 0 \tag{9}$$

（4）Discrepancy correction of multi-source SM products

To mitigate inconsistencies among passive microwave SM products from different satellite missions, we applied a pixel-wise linear regression correction using AMSR-E as the reference dataset. This approach harmonized SMOS and AMSR2 observations, resulting in a temporally consistent and spatially continuous SM dataset spanning 2003–2023, which was subsequently used for downscaling. The corrected SM value Y^* was calculated as:

$$Y^* = \mu_X + (Y - \mu_Y)C_Y \tag{10}$$

where X is the reference dataset (AMSR-E). Y is the original dataset (SMOS or AMSR2). μ_X and μ_Y are the temporal means of X and Y, respectively. The scaling factor C_Y is defined as:

$$C_Y = \rho_{XY}\sigma_X\sigma_Y \tag{11}$$

Here, σ_X and σ_Y are the standard deviations of X and Y, respectively, and ρ_{XY} is the Pearson correlation coefficient between the two datasets.

3.1.2. Downscaling of passive microwave remote sensing data

The temperature-vegetation dryness index (TVDI) serves as a robust proxy for SM estimation, with demonstrated efficacy in SM retrieval and downscaling applications. Meng et al. (2021) leveraged the negative correlation between TVDI and SM to develop a spatial weight decomposition (SWD) model based on TVDI, ultimately constructing a fine-resolution SM dataset for China. However, it is important to note that the relationship between TVDI and SM is inherently modulated by local climatic and topographic conditions (Meng et al., 2021). To account for the potential modulating effects of heterogeneous climatic and environmental covariates, including precipitation regimes, thermal gradients, topographic variations, vegetation, and insolation patterns, on the TVDI-SM relationship, we implemented a random forest (RF) algorithm. The RF model was trained using coarse-resolution TVDI observations and corresponding SM measurements across diverse bioclimatic zones to capture non-linear interactions between hydroclimatic drivers and SM dynamics. Subsequently, this optimized model was applied to fine-scale TVDI data integrated with high-resolution climatic and environmental covariates, enabling the generation of spatially enhanced SM estimates through feature-based downscaling.

（1）Calculation of the TVDI

TVDI derived from the triangular/trapezoidal feature space between LST and NDVI (Fig. 3), serves as a robust SM proxy by capturing soil moisture dynamics through the inverse coupling of thermal and vegetation signals (Meng et al., 2021; Huang et al., 2025). TVDI is mathematically defined as:

$$TVDI = \frac{T_s - (a_2 \times NDVI + b_2)}{(a_1 \times NDVI + b_1) - (a_2 \times NDVI + b_2)} \tag{12}$$

https://doi.org/10.5194/egusphere-2025-5122
Preprint. Discussion started: 24 November 2025

where T_s represents pixel-level LST. a_1, b_1 and a_2, b_2 denote the dry-edge and wet-edge regression coefficients, respectively. TVDI values range from 0 to 1, quantitatively reflecting SM variability across spatial gradients.

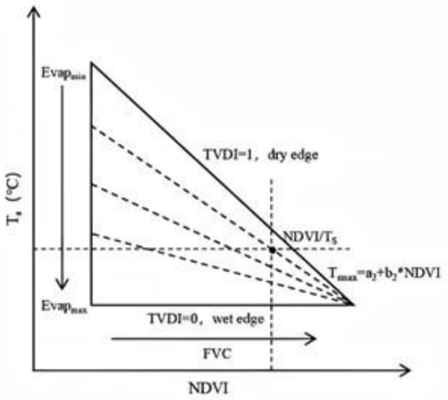

Fig. 3. LST and NDVI feature space diagram

(2) Construction of the RF

RF algorithm, an ensemble learning method grounded in bootstrap aggregation (bagging) and randomized feature subspace optimization, was implemented to model the non-linear interactions between SM and its environmental determinants, including TVDI, LAI, precipitation, 2m temperature, DEM, slope, evaporation, surface net solar radiation, and land cover (Breiman, 2001). During training, 500 decorrelated decision trees were constructed, each trained on a bootstrapped subset (80% of coarse-resolution data from 2003–2020) with node splits determined by optimal partitioning of a random feature subset. Hyperparameter tuning via grid search identified robust configurations: a minimum of 5 samples per leaf and unlimited tree depth to resolve complex SM-environment couplings (Biau, 2012). The model demonstrated high predictive accuracy, with an out-of-bag (OOB) R^2 of 0.956 and mean absolute error (MAE) of 0.027 m^3/m^3 on validation data. Permutation importance analysis identified TVDI, precipitation, surface net solar radiation, LAI, and land cover as dominant predictors.

For downscaling, the trained RF ingested high-resolution (0.05°) TVDI and environmental layers, generating fine-scale SM estimates through ensemble averaging. To ensure scale consistency between training (0.25°) and prediction (0.05°) domains, a multi-resolution feature alignment strategy was implemented: high-resolution covariates were aggregated to match the coarse training resolution using spatial averaging prior to model training, while native-resolution data were retained for prediction.

3.2. Identification and analysis of agricultural drought

(1) mapping of agricultural drought using SSI

SSI is recognized as one of the most effective indicators for assessing agricultural drought (Xu et al., 2018). To compute the SSI, pixel-wise time series analysis was conducted on the 2003–2023 China SM dataset. Five probability distribution functions—gamma, normal, log-normal, generalized extreme value, and pearson-III—were systematically evaluated for their fit to SM data using the Kolmogorov–Smirnov test (Svensson et al., 2017). The results indicated that the normal distribution provided the best fit for most SM time series across the study area ($p > 0.05$). The SSI was calculated as:

$$SSI = \frac{SM - \mu}{\sigma} \quad (13)$$

Where μ and σ represent the pixel-specific mean and standard deviation of monthly SM values over the 2003–2023 baseline period. Following world meteorological organization guide lines and regional agricultural vulnerability thresholds (Svoboda et al., 2012), drought severity was classified into five categories (Table 2).

Table 2 SSI-based drought severity classification

SSI Range	Drought Category
SSI > 0	Non dryness
-1.0 < SSI ≤ 0	Mild dryness
-1.5 < SSI ≤ -1.0	Moderate dryness
-2.0 < SSI ≤ -1.5	Severe dryness
SSI ≤ -2.0	Extreme dryness

（2）Analysis of drought trends and characteristics

Agricultural drought trends across China were quantified using the non-parametric Sen's slope estimator and Mann-Kendall (M–K) test, a robust approach for detecting monotonic trends in climate time series (Han et al., 2023).

(i) Sen's slope estimation

The Sen's slope estimator determines the median rate of change between all pairwise combinations in a time series, offering resistance to outliers and distribution-free computation. For a time series of *n* observations $(x_1, x_2, \ldots, x_n)$, the slope is calculated as:

$$Slope = \text{Median}(\frac{x_j - x_i}{j - i}), \qquad \forall 1 \le i \le j \le n \quad (14)$$

Where x_i and x_j denote the i^{th} and j^{th} observations of the time series, respectively. $Median$ denotes the median function. The estimated slope indicates the average rate of change. A positive slope suggests an increasing trend, a negative slope indicates a decreasing trend, and a slope of zero implies no significant trend.

(ii) M–K trend test

The M–K test is a non-parametric method used to detect monotonic trends in time series data, which does not assume any specific distribution and is insensitive to a few outliers. The null hypothesis assumes that the observations$x_1, x_2, \ldots, x_n$ are independent and identically distributed, while the alternative hypothesis posits the existence of a monotonic trend. The test statistic S is calculated as:

$$S = \sum_{k=1}^{n-1} \sum_{j=k+1}^{n} \text{sgn}(x_j - x_k) \quad (15)$$

where the sign function is defined as:

$$\text{sgn}(x_j - x_k) = \begin{cases} 1 & (x_j - x_k > 0) \\ 0 & (x_j - x_k = 0) \\ -1 & (x_j - x_k < 0) \end{cases} \quad (16)$$

Under the null hypothesis, S approximately follows a normal distribution with mean zero and variance:

https://doi.org/10.5194/egusphere-2025-5122
Preprint. Discussion started: 24 November 2025

$$\mathrm{Var}(S) = \frac{n(n-1)(2n+5)}{18} \quad (17)$$

For $n > 10$, the standardized test statistic Z is given by:

$$Z = \begin{cases} \frac{S-1}{\sqrt{\mathrm{Var}(S)}} & (S > 0) \\ 0 & (S = 0) \\ \frac{S+1}{\sqrt{\mathrm{Var}(S)}} & (S < 0) \end{cases} \quad (18)$$

At a given significance level α, if $|Z| \geq Z_{1-\alpha/2}$, the null hypothesis is rejected, indicating a statistically significant trend. A positive Z denotes an increasing trend, while a negative Z indicates a decreasing trend. Specifically, $|Z| \geq 1.96$ and $|Z| \geq 2.58$ correspond to significance levels of 95% and 99%, respectively.

4.Result

4.1. Evaluation and validation of downscaled SM

The downscaled SM product (with a 0.05° resolution) preserved the spatial pattern of the original 0.25° dataset, including the dominant northwest-to-southeast moisture gradient, while significantly enhancing the representation of localized hydrological heterogeneity (Fig. 4). For instance, along the 28.9°N latitudinal transect, the downscaled SM data effectively capture the west-to-east fluctuations and exhibit heightened sensitivity to small-scale variations. Furthermore, exhibits a more detailed texture and sharper gradient transitions, particularly in heterogeneous zones like the cropland-forest ecotone, where it provides a more accurate reflection of soil moisture's spatial heterogeneity. As shown in the zoomed-in area of Fig. 4, critical subgrid features that were previously obscured in passive microwave observations are now resolved with a precision of 0.038 m^3/m^3.

https://doi.org/10.5194/egusphere-2025-5122
Preprint. Discussion started: 24 November 2025

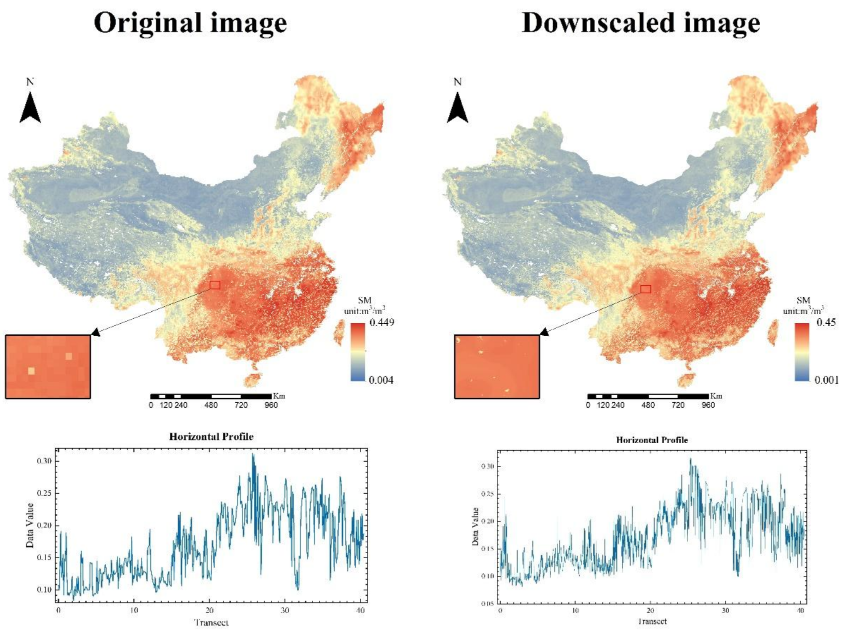

Fig. 4. Comparison of original images and downscaled SM images.

The accuracy of the downscaled SM product was rigorously evaluated across nine major river basins using the correlation coefficient (R), unbiased root mean square error (ubRMSE), and bias (Fig. 5). The downscaled SM exhibited strong agreement with in-situ observations, with ubRMSE values ranging from 0.022 to 0.039 m³/m³ and R values from 0.777 to 0.919. More than 92% of validation points were tightly clustered along the 1:1 line, indicating a high level of accuracy in capturing ground-based SM variability. However, due to the strong spatial heterogeneity of SM in the study area, a single ground observation site is insufficient to fully represent the true SM conditions at the 0.05° grid scale. This scale effect leads to deviations of some validation points from the 1:1 line, particularly in regions with complex vegetation cover and significant topographic variation.

https://doi.org/10.5194/egusphere-2025-5122
Preprint. Discussion started: 24 November 2025

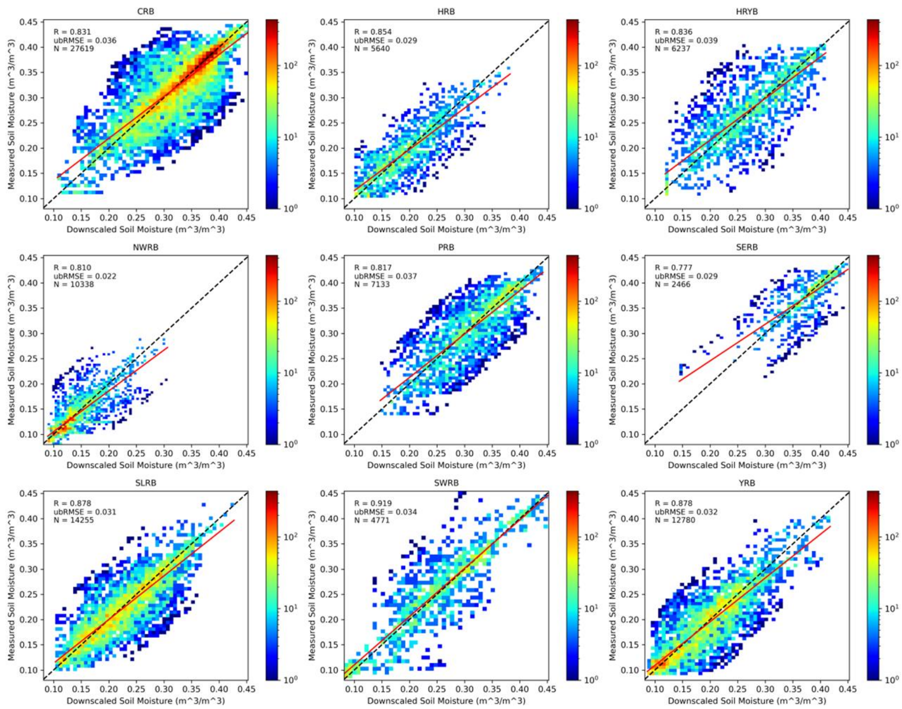

Fig. 5. Validation of downscaled SM against in situ measurements across nine major river basins. Scatterplot points are colored by kernel density estimates, with the red solid line indicating linear regression and the black dashed line representing the 1:1 relationship.

A comparative analysis was conducted to further evaluate the performance of the downscaled SM product against the original 0.25°-resolution product (PIII) and two benchmark datasets: Zhang et al., (2023)'s global 1 km-resolution SM product (PI) and Meng et al., (2021)'s 0.05°-resolution SM product (PII). The downscaling algorithm significantly enhanced SM accuracy across all land cover types, reducing the ubRMSE by 5.6–43.4% (e.g., from 0.053 to 0.030 $m^3\ m^{-3}$ in shrublands areas) and improving the R by 4.2–50% ($p<0.05$, paired t-test) compared to PIII. Notably, our product outperformed PII across all seven land cover classes, achieving significant ubRMSE reductions in complex surfaces: urban (11.9%), shrubland (14.3%), grassland (14.3%), and barren (12.8%) regions. Compared to PI, although our product has a coarser resolution (0.05° vs. 1 km), it demonstrated comparable or even superior accuracy in several areas due to regionally optimized parameters that account for China-specific hydroclimatic drivers. This underscores the critical role of localized algorithm calibration in mitigating biases from generic global models. Overall, the validation results indicate that the developed downscaled SM product offers high accuracy and broad applicability across China, supporting its potential for use in fine-scale agricultural drought monitoring.

https://doi.org/10.5194/egusphere-2025-5122
Preprint. Discussion started: 24 November 2025

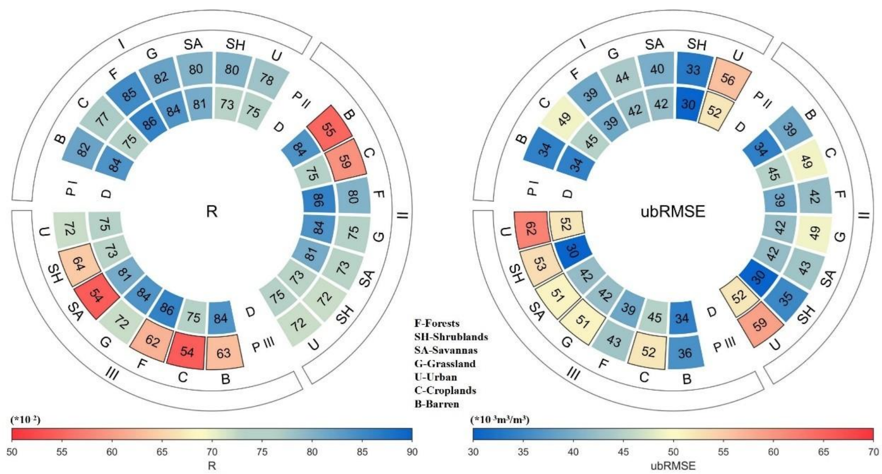

Fig. 6. Accuracy comparison of the downscaled SM product against three benchmark datasets—PI (Zhang et al., 2023), PII (Meng et al., 2021), and PIII (original coarse-resolution product)—across land cover types and river basins. Left: R, Right: ubRMSE (m^3 m^{-3}). Inner labels represent land cover categories (F: Forests, SH: Shrublands, SA: Savannas, G: Grasslands, U: Urban, C: Croplands, B: Barren).

4.2. Evaluation of drought index

As the primary victims of agricultural drought, crops serve as a direct and effective indicator for evaluating the accuracy of drought monitoring indices (Raza et al., 2019). In this study, the applicability of the SSI for agricultural drought monitoring was assessed by comparing its temporal dynamics with officially reported crop drought-affected areas across representative provinces (including municipalities and autonomous regions) within China's nine major river basins (Fig. 7). Temporal analysis revealed significant negative correlations between area-averaged SSI and governmental crop drought-affected areas (Pearson's R=0.015 to 0.277, p<0.05), with years of widespread drought (e.g., 2006, 2008, 2013, 2018, and 2022 in Hubei province) consistently coinciding with SSI minima (SSI<−2.0). These results demonstrate that the SSI derived from downscaled SM data can effectively capture agricultural drought patterns across China.

https://doi.org/10.5194/egusphere-2025-5122
Preprint. Discussion started: 24 November 2025

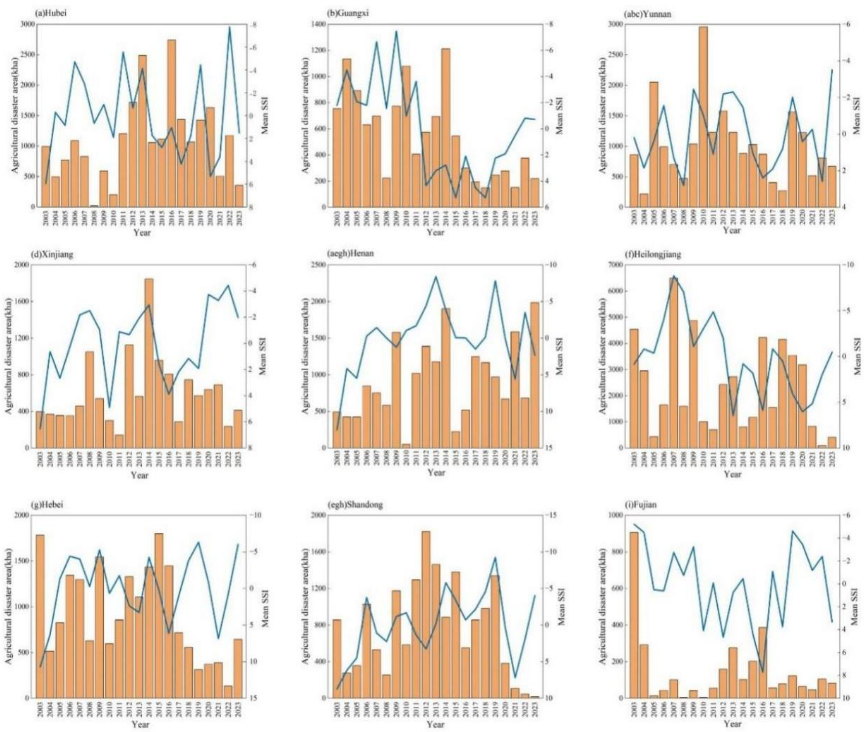

Fig. 7. Interannual variability of SSI and officially reported crop drought-affected areas (2003–2023) in selected provinces across nine major river basins in China. The subplot labels (a–i) correspond to the following river basins: (a) CRB, (b) PRB, (c) SWRB, (d) NWRB, (e) YRB, (f) SLRB, (g) HRB, (h) HRYB, and (i) SERB. Province-level administrative units spanning multiple basins are denoted by combined letters (e.g., abe= overlap of CRB, PRB and YRB).

4.3. SSI-based drought characterization

Fig. 8 depicts the spatiotemporal evolution of agricultural drought across China from 2003 to 2023, quantified through the annual mean SSI and drought-affected cropland area. Nationally aggregated SSI exhibited a "decline-rise-decline" trajectory (Fig. 8a), with a net decrease of 0.26 over the study period ($p < 0.05$), signaling progressive drought intensification. Spatially, Sen's slope estimation combined with M-K trend tests revealed heterogeneous drying patterns (Fig. 8b): significant SSI declines ($p < 0.1$) dominated the YRB, HRB, NWRB, and southwestern part of YRB, peaking at the HRB-YRB-SLRB tri-junction (-0.056 yr^{-1}, $p < 0.05$). Contrastingly, northeastern part of SLRB and the southwestern part of PRB showed SSI increases ($p < 0.05$), indicating localized moisture recovery. These trends formed distinct spatial gradients—a weakening northwest-to-southeast drying gradient (from -0.124 yr^{-1} in arid zones to 0.053 yr^{-1} in humid coasts) and an intensifying northeast-to-southwest aridity trend aligned with monsoonal boundary shifts. The tri-junction hotspot's accelerated drying correlated with compounding drivers: The tri-junction hotspot's accelerated drying is correlated with compounding drivers: significant groundwater depletion (−2.37 mm/yr from 2002 to 2023), substantial irrigation expansion in the region, and warming rates that exceed national averages (Liang et al., 2024). This spatial heterogeneity

https://doi.org/10.5194/egusphere-2025-5122
Preprint. Discussion started: 24 November 2025

underscores the imperative for regionally adaptive drought management strategies under changing hydroclimatic regimes.

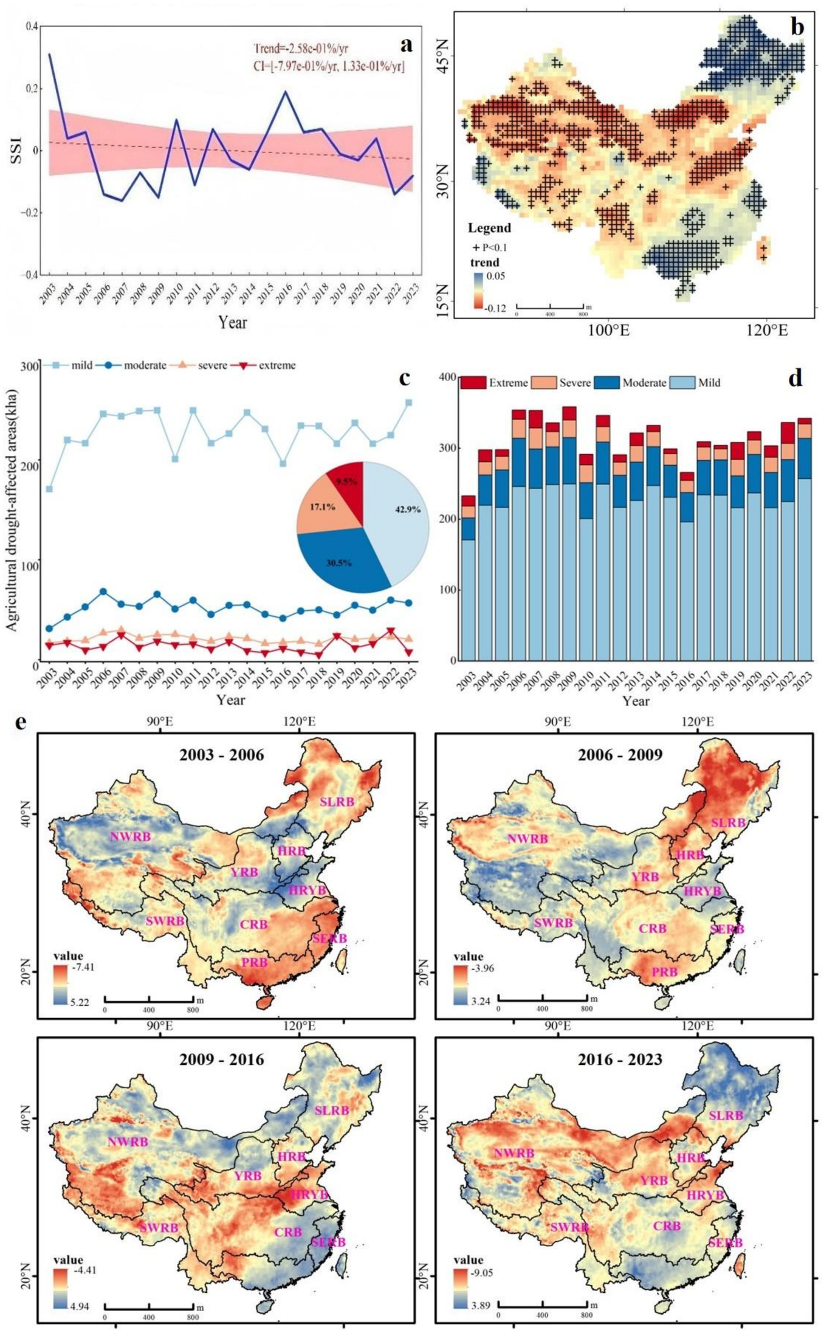

Fig. 8. Spatiotemporal evolution of agricultural drought across China from 2003 to 2023. (a) Interannual variation of annual mean SSI in China, (b) Sen's slope estimation and Mann–Kendall trend test of SSI,

https://doi.org/10.5194/egusphere-2025-5122
Preprint. Discussion started: 24 November 2025

(c) interannual variations in drought-affected cropland area categorized by severity levels (mild, moderate, severe, extreme), and (d–e) four characteristic stages of drought evolution.

The hierarchical structure of drought severity (Fig. 8c) revealed persistent dominance of mild droughts (43% of total affected area), which expanded significantly at 0.677×10^3 kha/yr ($p< 0.05$), while severe and extreme droughts collectively accounted for 30% but declined slightly at -0.258×10^3 kha/yr ($p< 0.05$). The proportional contributions of different drought severity categories followed a 4:3:2:1 ratio (mild: moderate: severe: extreme), reflecting a pyramidal drought severity distribution. Drought evolution from 2003 to 2023 progressed through four distinct phases (Figures 8d–e): (1) 2003–2006 (drought intensification phase): Droughts were predominantly concentrated in southern China, particularly in the PRB, SERB, and the northern part of the CRB, exhibiting a spatial pattern of higher drought prevalence in the south than in the north, with weaker severity in the west and stronger severity in the east. (2) 2006–2009 (drought outbreak phase): Annual drought-affected areas exceeded 32.8×10^4 km^2, with severe and extreme droughts accounting for over 26%, mainly concentrated in northern major grain-producing regions such as SLRB, YRB, and HRB. (3) 2009–2016 (drought transition phase): Mild drought area fluctuated downward, while moderate and severe drought areas increased by 12% and 9%, respectively. Extreme droughts remained stable at around 4%, and the drought center shifted toward HRYB agricultural core. (4) 2016–2023 (drought intensification phase): All drought categories increased, with mild droughts expanding most rapidly (accounting for ~51%). Compared to the previous phase, the drought center migrated further northward.

The intra-annual variation of the SSI across China (Fig. 9a) exhibits a bimodal seasonal pattern, characterized by two distinct drought peaks in spring (March–May) and late autumn to early winter (October–December). Drought intensity tends to escalate progressively throughout these periods. Monthly mean SSI values range from -0.2 to 0.33, with mild drought conditions dominating nationally. SSI values fall below the drought threshold (SSI<0) in seven months, with the lowest values observed in April (-0.193) and December (-0.172), marking the driest periods of the year. In contrast, during June to September, enhanced summer monsoon precipitation contributes to wetter conditions, as reflected by predominantly positive SSI values and markedly reduced drought frequency. The spatio–temporal distribution of drought demonstrates considerable regional heterogeneity (Fig. 9b). From January to June, drought patterns expand from southwest to northeast, while during the second half of the year, the dry zones extend from the YRB–HRB toward the northwest and southeast. The southern part of the NWRB, SWRB, and northern part of the CRB exhibit a seasonal cycle of "winter–spring drought and summer–autumn wetness," primarily driven by limited winter–spring precipitation and increased evapotranspiration across highland regions (Zhu et al., 2015). The SLRB experiences frequent large-scale drought events during late autumn to early winter and again in late spring to early summer, with May and November showing the most pronounced dryness. The HRYB, HRB, and YRB are characterized by spring drought dominance. In contrast, droughts in the eastern CRB and SERB mainly occur in summer and autumn, with October exhibiting the lowest SSI values of the year, indicating heightened risk of moderate to severe drought events. The PRB is predominantly affected by drought during late autumn and early winter, with a high likelihood of moderate droughts occurring during this transitional period.

https://doi.org/10.5194/egusphere-2025-5122
Preprint. Discussion started: 24 November 2025

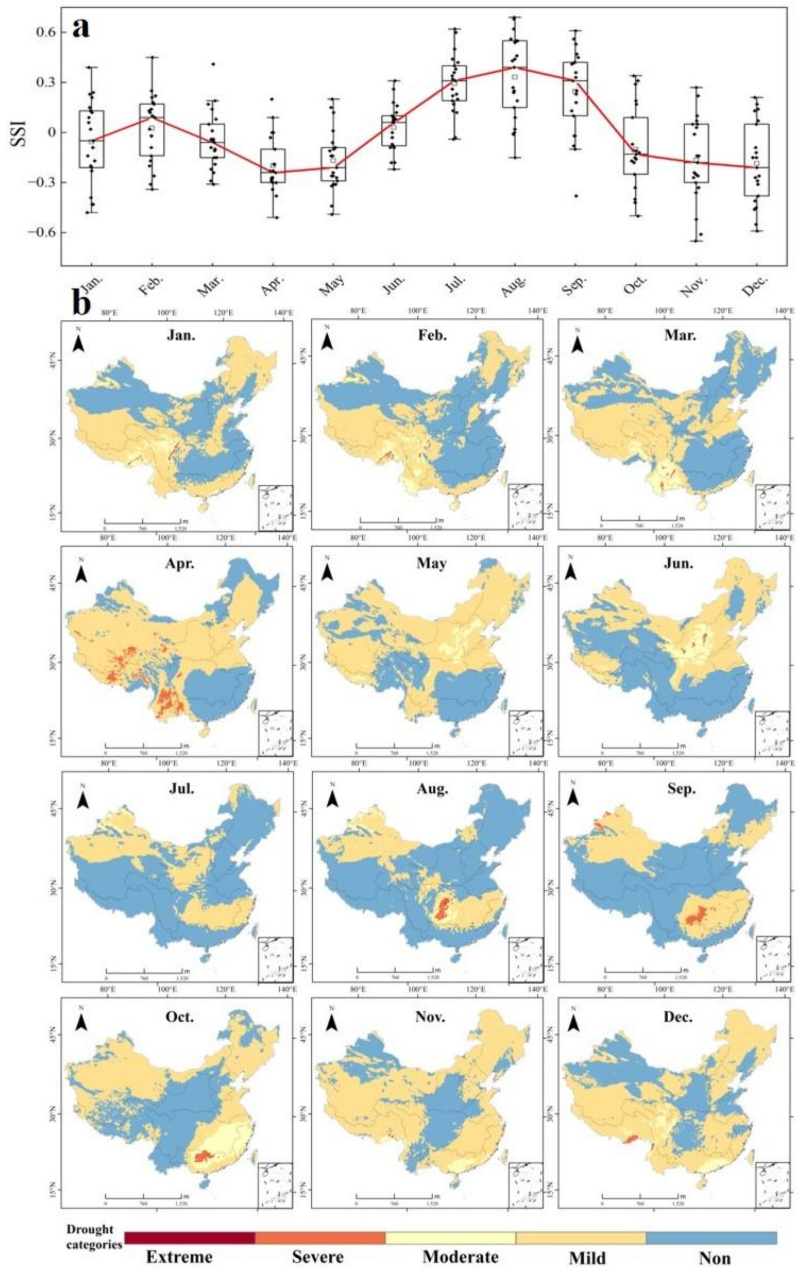

Fig. 9. Intra-annual variability and spatiotemporal evolution of agricultural drought in China (2003–2023) based on the SSI. (a) Boxplots of intra-annual variation of multi-year mean SSI across China, (b) Temporal evolution of spatial patterns of agricultural drought in China.

Fig. 10 illustrates the spatial distribution of annual agricultural drought frequency across China from 2003 to 2023. Approximately 92% of the territory experienced agricultural drought events during this period, with drought frequencies ranging from 32% to 52%, indicating a high

https://doi.org/10.5194/egusphere-2025-5122
Preprint. Discussion started: 24 November 2025

spatiotemporal prevalence of agricultural droughts in China. The spatial distribution of agricultural droughts exhibits significant heterogeneity, with a general pattern of higher frequency in the northwest and lower frequency in the southeast, aligning closely with the climate gradient where precipitation decreases from southeast to northwest (Xu et al., 2015). High-frequency drought areas are primarily concentrated in the NWRB, HRB, and YRB, where the annual drought occurrence frequency exceeds 48%. In specific regions such as the middle and upper reaches of Ningxia, central and western Inner Mongolia, and northern Shanxi, the frequency can reach up to 75%. Drought frequencies in the SLRB, HRYB, PRB, and SWRB range from 42% to 50% annually. The CRB and SERB exhibit the lowest frequencies, with the central and eastern CRB experiencing drought occurrence rates of approximately 15%. Notably, areas with high drought frequency (>50%) overlap significantly with China's key agro-pastoral transition zones and ecologically vulnerable regions, a pattern likely linked to anomalies in westerly winds and reduced monsoon precipitation (Fang et al., 2020), highlighting the increased vulnerability of these regions to drought stress.

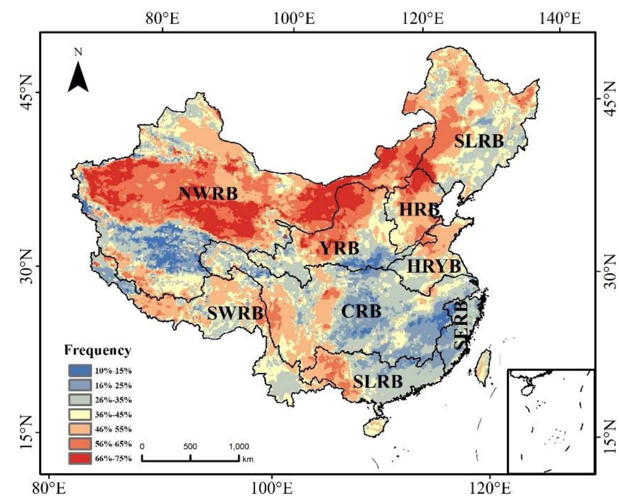

Fig. 10. Spatiotemporal characteristics of annual agricultural drought frequency in China (2003-2023).

5.Discussion and conclusion

Agricultural drought directly affects regional agricultural productivity and livelihoods. As a key indicator of agricultural drought, SM plays a critical role in determining monitoring accuracy. Although the temporal resolution of global remote sensing SM datasets continues to improve, they often suffer from spatiotemporal gaps due to factors such as orbital limitations and cloud cover (Albergel et al., 2012; Korpela et al., 2012). Our study addresses these limitations by integrating multi-source SM data with a spatiotemporally adaptive reconstruction framework and machine learning-based downscaling, generating a seamless 0.05° resolution SM product for China from 2003 to 2023. The dataset demonstrates significant improvements over conventional products, with a 25–59% reduction in ubRMSE and enhanced capacity to resolve subgrid features such as urban and forest edges. Validation against 2,411 in situ stations confirms robust accuracy (R=0.89, ubRMSE = 0.029 m^3/m^3), particularly in ecologically fragile transition zones where global datasets fail to capture localized moisture gradients.

Using the SSI, we identified a bimodal seasonal drought pattern: spring (March–May) and autumn-winter (October–December) peaks, may be driven by monsoon delays in the north and

https://doi.org/10.5194/egusphere-2025-5122
Preprint. Discussion started: 24 November 2025

subtropical high retreat in the south (Xu et al., 2015). In addition, agricultural drought in China has shown a general intensifying trend since 2003, with drought severity generally decreasing from northwest to southeast, and increasing from northeast to southwest. High-frequency drought zones were predominantly clustered in ecologically vulnerable regions, particularly the agro-pastoral ecotone of northern China. Although northwest China has exhibited a "warming and wetting" trend in recent years, this effect is largely confined to northern Xinjiang. In contrast, regions such as southern Xinjiang and Gansu still experience potential evapotranspiration that far exceeds precipitation, resulting in a continued trend toward intensifying drought (Deng et al., 2022). Notably, drought cores have migrated northward since 2003, aligning with monsoon belt shifts and intensified groundwater depletion in the Yellow River Basin and North China Plain (Yang et al., 2015; Chen et al., 2023; Zhou et al., 2023). These findings highlight the urgent need for regionally adaptive drought management strategies, particularly in spring-drought-prone northern plains and ecologically fragile ecotones where groundwater overexploitation exacerbates moisture stress.

Although using SSI and generated SM product achieved quantitative mapping from SM to drought severity, and validation based on regional drought-affected areas suggests that the method effectively captures spatial drought characteristics across China. However, the study remains constrained by input parameter quality and static SSI thresholds, particularly in regions with complex terrain and mixed land cover. Future advancements in high-resolution environmental covariates (e.g., evapotranspiration, irrigation maps) could further refine SM estimates and help to develop dynamic drought thresholds.

https://doi.org/10.5194/egusphere-2025-5122
Preprint. Discussion started: 24 November 2025

Data availability statement: The shapefile boundary data used in this study were obtained from the Resource and Environmental Science and Data Center of the Chinese Academy of Sciences (https://www.resdc.cn/data.aspx?DATAID=141). Monthly soil moisture products from AMSR-E aboard the Aqua satellite and AMSR2 aboard the GCOM-W1 satellite were acquired from the NASA Earthdata Search platform (https://search.earthdata.nasa.gov/search). The SMOS-IC V105 soil moisture dataset was accessed from the CATDS (https://www.catds.fr/Products/Products-over-Land/SMOS-IC). In-situ soil moisture observations from January 2003 to December 2023 were sourced from the China Meteorological Administration and Agricultural Meteorological Stations (https://data.cma.cn/). Reanalysis datasets were obtained from the European Centre for Medium-Range Weather Forecasts (ECMWF) via the Copernicus Climate Data Store (https://cds.climate.copernicus.eu/datasets). Land cover and auxiliary remote sensing datasets were retrieved from the NASA LP DAAC (https://lpdaac.usgs.gov/). Statistical yearbook data used for agricultural drought assessment were obtained from the National Bureau of Statistics of China (https://www.stats.gov.cn/sj/ndsj/).

Author contribution: MC and YC: Data curation, Investigation, Methodology, Writing. XL, YZ, YY and XM: Conceptualization, Methodology, Formal analysis, Investigation.

Declaration of competing interest: The authors declare no competing financial interests.

Acknowledgments: The authors extend their heartfelt appreciation to Google for their invaluable contribution of the open-source machine learning framework, and TensorFlow for offering the sophisticated machine learning library that served as the cornerstone for conducting these experiments. This study is funded by the following projects: National Natural Science Foundation of China (No.42071415), Central Plains Youth Top Talent Project, University Science and Technology Innovation Team in Henan Province (No. 25IRTSTHN004), Postgraduate Education Reform and Quality Improvement Project of Henan Province (No. YJS2023JC22), Xinyang Academy of Ecological Research Open Foundation (No.2023XYMS01), the National Civil Space Infrastructure 13th Five-Year Plan for Common Application Support Platform of Terrestrial Observation Satellites and the Natural Science Foundation of Henan (252300420827).

References

Aiguo, D., 2011. Characteristics and trends in various forms of the Palmer Drought Severity Index during 1900–2008. Journal of Geophysical Research 116, 115–123. https://doi.org/10.1029/2010JD015541

Albergel, C., De Rosnay, P., Gruhier, C., Muñoz-Sabater, J., Hasenauer, S., Isaksen, L., Kerr, Y., Wagner, W., 2012. Evaluation of remotely sensed and modelled soil moisture products using global ground-based in situ observations. Remote Sensing of Environment 118, 215–226. https://doi.org/10.1016/j.rse.2011.11.017

Biau, G., 2012. Analysis of a Random Forests Model. Journal of Machine Learning Research 13, 1063–1095. https://doi.org/10.1145/2188385.2343682

Bodner, G., Nakhforoosh, A., Kaul, H.-P., 2015. Management of crop water under drought: a review. Agronomy for Sustainable Development 35, 401–442. https://doi.org/10.1007/s13593-015-0283-4

Breiman, L., 2001. Random forests. Machine Learning 45, 5–32. https://doi.org/10.1023/A:1010933404324

Cao, M., Mao, K., Yan, Y., Shi, J., Wang, H., Xu, T., Fang, S., Yuan, Z., 2021. A new global gridded sea surface temperature data product based on multisource data. Earth System Science Data 13, 2111–2134. https://doi.org/10.5194/essd-13-2111-2021

Chen, Fahu, Xie, T., Yang, Y., Chen, S., Chen, Feng, Huang, W., Chen, J., 2023. Discussion of the "warming and wetting" trend and its future variation in the drylands of Northwest China under global warming. Science China Earth Sciences. 66, 1241–1257. https://doi.org/10.1007/s11430-022-1098-x

Chen, Y., Cao, R., Chen, J., Liu, L., Matsushita, B., 2021. A practical approach to reconstruct high-quality Landsat NDVI time-series data by gap filling and the Savitzky–Golay filter. ISPRS Journal of Photogrammetry and Remote Sensing 180, 174–190. https://doi.org/10.1016/j.isprsjprs.2021.08.015

Dai, A., 2013. Increasing drought under global warming in observations and models. Nature Climate Change 3, 52–58. https://doi.org/10.1038/nclimate1633

Deng, H., Tang, Q., Yun, X., Tang, Y., Liu, X., Xu, X., Sun, S., Zhao, G., Zhang, Yongyong, Zhang, Yongqiang, 2022. Wetting trend in Northwest China reversed by warmer temperature and drier air. Journal of Hydrology 613, 128435. https://doi.org/10.1016/j.jhydrol.2022.128435

Ding, T., Zhao, W., Yang, Y., 2024. Addressing spatial gaps in ESA CCI soil moisture product: A hierarchical reconstruction approach using deep learning model. International Journal of Applied Earth Observation and Geoinformation 132, 104003. https://doi.org/10.1016/j.jag.2024.104003

Dong, J., Crow, W.T., Tobin, K.J., Cosh, M.H., Bosch, D.D., Starks, P.J., Seyfried, M., Collins, C.H., 2020. Comparison of microwave remote sensing and land surface modeling for surface soil moisture climatology estimation. Remote Sensing of Environment 242, 111756. https://doi.org/10.1016/j.rse.2020.111756

Fang, W., Huang, S., Huang, Q., Huang, G., Wang, H., Leng, G., Wang, L., 2020. Identifying drought propagation by simultaneously considering linear and nonlinear dependence in the Wei River basin of the Loess Plateau, China. Journal of Hydrology 591, 125287. https://doi.org/10.1016/j.jhydrol.2020.125287

Fuentes, I., Padarian, J., Vervoort, R.W., 2022. Towards near real-time national-scale soil water

content monitoring using data fusion as a downscaling alternative. Journal of Hydrology 609, 127705. https://doi.org/10.1016/j.jhydrol.2022.127705
Hansen, J.W., Jones, J.W., 2000. Scaling-up crop models for climate variability applications. Agricultural Systems 65, 43–72. https://doi.org/10.1016/S0308-521X(00)00025-1
Huang, D., Ma, T., Liu, J., Zhang, J., 2025. Agricultural drought monitoring using modified TVDI and dynamic drought thresholds in the upper and middle Huai River Basin, China. Journal of Hydrology: Regional Studies 57, 102069. https://doi.org/10.1016/j.ejrh.2024.102069
Imaoka, K., Kachi, M., Kasahara, M., Ito, N., Nakagawa, K., Oki, T., 2010. Instrument performance and calibration of AMSR-E and AMSR2. International Archives of the Photogrammetry Remote Sensing and Spatial Information Sciences 38, 13–16.
Han, J., Gelata, F.T., Chaka Gemeda, S., 2023. Application of MK trend and test of Sen's slope estimator to measure impact of climate change on the adoption of conservation agriculture in Ethiopia. Journal of Water and Climate Change 14, 977–988. https://doi.org/10.2166/wcc.2023.508
Kandasamy, S., Baret, F., Verger, A., Neveux, P., Weiss, M., 2013. A comparison of methods for smoothing and gap filling time series of remote sensing observations – application to MODIS LAI products. Biogeosciences 10, 4055–4071. https://doi.org/10.5194/bg-10-4055-2013
Konings, A.G., Rao, K., Steele-Dunne, S.C., 2019. Macro to micro: microwave remote sensing of plant water content for physiology and ecology. New Phytologist 223, 1166–1172. https://doi.org/10.1111/nph.15808
Korpela, I., Hovi, A., Morsdorf, F., 2012. Understory trees in airborne LiDAR data — Selective mapping due to transmission losses and echo-triggering mechanisms. Remote Sensing of Environment 119, 92–104. https://doi.org/10.1016/j.rse.2011.12.011
Liang, H., Zhou, Y., Cui, Y., Dong, J., Gao, Z., Liu, B., Xiao, X., 2024. Is satellite-observed surface water expansion a good signal to China's largest granary? Agricultural Water Management 303, 109039. https://doi.org/10.1016/j.agwat.2024.109039
Liu, C., Yang, C., Yang, Q., Wang, J., 2021. Spatiotemporal drought analysis by the standardized precipitation index (SPI) and standardized precipitation evapotranspiration index (SPEI) in Sichuan Province, China. Scientific Reports 11, 1280. https://doi.org/10.1038/s41598-020-80527-3
Liu, W., Wang, J., Xu, F., Li, C., Xian, T., 2022. Validation of Four Satellite-Derived Soil Moisture Products Using Ground-Based In Situ Observations over Northern China. Remote Sensing 14, 1419. https://doi.org/10.3390/rs14061419
Malbéteau, Y., Merlin, O., Molero, B., Rüdiger, C., Bacon, S., 2016. DisPATCH as a tool to evaluate coarse-scale remotely sensed soil moisture using localized in situ measurements: Application to SMOS and AMSR-E data in Southeastern Australia. International Journal of Applied Earth Observation and Geoinformation 45, 221–234. https://doi.org/10.1016/j.jag.2015.10.002
Meng, X., Mao, K., Meng, F., Shi, J., Zeng, J., Shen, X., Cui, Y., Jiang, L., Guo, Z., 2021. A fine-resolution soil moisture dataset for China in 2002–2018. Earth System Science Data 13, 3239–3261. https://doi.org/10.5194/essd-13-3239-2021
Meng, X., Peng, J., Hu, J., Li, J., Leng, G., Ferhatoglu, C., Li, X., García-García, A., Yang, Y., 2024. Validation and expansion of the soil moisture index for assessing soil moisture dynamics

https://doi.org/10.5194/egusphere-2025-5122
Preprint. Discussion started: 24 November 2025

from AMSR2 brightness temperature. Remote Sensing of Environment 303, 114018. https://doi.org/10.1016/j.rse.2024.114018

Merlin, O., Rudiger, C., Al Bitar, A., Richaume, P., Walker, J.P., Kerr, Y.H., 2012. Disaggregation of SMOS Soil Moisture in Southeastern Australia. IEEE Transactions on Geoscience and Remote Sensing 50, 1556–1571. https://doi.org/10.1109/TGRS.2011.2175000

Mohseni, F., Jamali, S., Ghorbanian, A., Mokhtarzade, M., 2023. Global soil moisture trend analysis using microwave remote sensing data and an automated polynomial-based algorithm. Global and Planetary Change 231, 104310. https://doi.org/10.1016/j.gloplacha.2023.104310

Ochsner, T.E., Cosh, M.H., Cuenca, R.H., Dorigo, W.A., Draper, C.S., Hagimoto, Y., Kerr, Y.H., Larson, K.M., Njoku, E.G., Small, E.E., Zreda, M., 2013. State of the Art in Large-Scale Soil Moisture Monitoring. Soil Science Society of America Journal 77, 1888–1919. https://doi.org/10.2136/sssaj2013.03.0093

Peng, J., Loew, A., Merlin, O., Verhoest, N.E.C., 2017. A review of spatial downscaling of satellite remotely sensed soil moisture. Reviews of Geophysics 55, 341–366. https://doi.org/10.1002/2016RG000543

Piles, M., Sanchez, N., Vall-llossera, M., Camps, A., Martinez-Fernandez, J., Martinez, J., Gonzalez-Gambau, V., 2014. A Downscaling Approach for SMOS Land Observations: Evaluation of High-Resolution Soil Moisture Maps Over the Iberian Peninsula. IEEE Journal of Selected Topics in Applied Earth Observations and Remote Sensing 7, 3845–3857. https://doi.org/10.1109/JSTARS.2014.2325398

Raza, A., Razzaq, A., Mehmood, S.S., Zou, X., Zhang, X., Lv, Y., Xu, J., 2019. Impact of Climate Change on Crops Adaptation and Strategies to Tackle Its Outcome: A Review. Plants 8, 34. https://doi.org/10.3390/plants8020034

Schmid, M., Rath, D., Diebold, U., 2022. Why and How Savitzky–Golay Filters Should Be Replaced. ACS Measurement Science Au 2, 185–196. https://doi.org/10.1021/acsmeasuresciau.1c00054

Song, P., Zhang, Y., Guo, J., Shi, J., Zhao, T., Tong, B., 2022. A 1 km daily surface soil moisture dataset of enhanced coverage under all-weather conditions over China in 2003–2019. Earth System Science Data 14, 2613–2637. https://doi.org/10.5194/essd-14-2613-2022

Song, P., Zhao, T., Shi, J., Zhang, Y., Zheng, J., 2024. A Novel Downscaling Approach Based on Multifrequency Microwave Radiometry Toward Finer Scale Global Soil Moisture Mapping. IEEE Transactions on Geoscience and Remote Sensing 62, 1–15. https://doi.org/10.1109/TGRS.2024.3490758

Sridhar, V., Hubbard, K.G., You, J., Hunt, E.D., 2008. Development of the Soil Moisture Index to Quantify Agricultural Drought and Its “User Friendliness” in Severity-Area-Duration Assessment. Journal of Hydrometeorology 9, 660–676. https://doi.org/10.1175/2007JHM892.1

Svensson, C., Hannaford, J., Prosdocimi, I., 2017. Statistical distributions for monthly aggregations of precipitation and streamflow in drought indicator applications. Water Resources Research 53, 999–1018. https://doi.org/10.1002/2016WR019276

Svoboda, M., Hayes, M., Wood, D., 2012. Standardized Precipitation Index: User Guide.

Wang, J., 2010. Food Security, Food Prices and Climate Change in China: a Dynamic Panel Data Analysis. Agriculture and Agricultural Science Procedia 1, 321–324.

https://doi.org/10.5194/egusphere-2025-5122
Preprint. Discussion started: 24 November 2025

https://doi.org/10.1016/j.aaspro.2010.09.040

White, J.W., Andrade-Sanchez, P., Gore, M.A., Bronson, K.F., Coffelt, T.A., Conley, M.M., Feldmann, K.A., French, A.N., Heun, J.T., Hunsaker, D.J., Jenks, M.A., Kimball, B.A., Roth, R.L., Strand, R.J., Thorp, K.R., Wall, G.W., Wang, G., 2012. Field-based phenomics for plant genetics research. Field Crops Research 133, 101–112. https://doi.org/10.1016/j.fcr.2012.04.003

Xu, K., Yang, D., Yang, H., Li, Z., Qin, Y., Shen, Y., 2015. Spatio-temporal variation of drought in China during 1961–2012: A climatic perspective. Journal of Hydrology 526, 253–264. https://doi.org/10.1016/j.jhydrol.2014.09.047

Xu, Y., Wang, L., Ross, K., Liu, C., Berry, K., 2018. Standardized Soil Moisture Index for Drought Monitoring Based on Soil Moisture Active Passive Observations and 36 Years of North American Land Data Assimilation System Data: A Case Study in the Southeast United States. Remote Sensing 10, 301. https://doi.org/10.3390/rs10020301

Yang, S., Ding, Z., Li, Y., Wang, X., Jiang, W., Huang, X., 2015. Warming-induced northwestward migration of the East Asian monsoon rain belt from the Last Glacial Maximum to the mid-Holocene. Proceedings of the National Academy of Sciences of the United States of America 112, 13178–13183. https://doi.org/10.1073/pnas.1504688112

Yang, X., Lu, M., Wang, Yufei, Wang, Yiran, Liu, Z., Chen, S., 2021. Response Mechanism of Plants to Drought Stress. Horticulturae 7, 50. https://doi.org/10.3390/horticulturae7030050

Yao, X., Fu, B., Lü, Y., Sun, F., Wang, S., Liu, M., 2013. Comparison of Four Spatial Interpolation Methods for Estimating Soil Moisture in a Complex Terrain Catchment. Public Library of Science ONE 8, e54660. https://doi.org/10.1371/journal.pone.0054660

Zhang, Q., Yang, J., Wang, W., Ma, P., Lu, G., Liu, X., Yu, H., Fang, F., 2021. Climatic Warming and Humidification in the Arid Region of Northwest China: Multi-Scale Characteristics and Impacts on Ecological Vegetation. Journal of Meteorological Research 35, 113–127. https://doi.org/10.1007/s13351-021-0105-3

Zhang, Y., Liang, S., Ma, H., He, T., Wang, Q., Li, B., Xu, J., Zhang, G., Liu, X., Xiong, C., 2023. Generation of global 1 km daily soil moisture product from 2000 to 2020 using ensemble learning. Earth Syst. Sci. Data 15, 2055–2079. https://doi.org/10.5194/essd-15-2055-2023

Zhong, Y., Wei, Z., Miao, L., Wang, Y., Walker, J.P., Colliander, A., 2024. Downscaling Passive Microwave Soil Moisture Estimates Using Stand-Alone Optical Remote Sensing Data. IEEE Transactions on Geoscience and Remote Sensing 62, 1–19. https://doi.org/10.1109/TGRS.2024.3386967

Zhou, Y., Dong, J., Cui, Y., Zhao, M., Wang, X., Tang, Q., Zhang, Y., Zhou, S., Metternicht, G., Zou, Z., Zhang, G., Xiao, X., 2023. Ecological restoration exacerbates the agriculture-induced water crisis in North China Region. Agricultural and Forest Meteorology 331, 109341. https://doi.org/10.1016/j.agrformet.2023.109341

Zhu, L., Gong, H., Dai, Z., Xu, T., Su, X., 2015. An integrated assessment of the impact of precipitation and groundwater on vegetation growth in arid and semiarid areas. Environmental Earth Sciences 74, 5009–5021. https://doi.org/10.1007/s12665-015-4513-5